GSA Data Repository Item 2019099

Synoptic view of lithospheric S-wave velocity structure in the southern United States: A comparison of 3-D seismic tomographic models

A. Netto, J. Pulliam, and P. Persaud

VELOCITY MODELS

Here we review the data types and methods used to generate the models compared in this study. A large proportion of the seismic data used by the studies derives from the USArray's Transportable Array (TA), which have a nominal station spacing of ~70 km. Readers interested in the locations of the USArray stations are directed to the IRIS DMC's USArray website (http://ds.iris.edu/ds/nodes/dmc/earthscope/usarray/).

DNA13

DNA13, by Porritt et al. (2014), combines teleseismic P, SH, and SV observations and surface wave phase velocities from 400 teleseismic earthquakes, 167 local earthquakes, and ambient noise, recorded between January 2007 and December 2012, using the joint inversion method of Obrebski et al. (2011). Body-wave traveltimes were measured by multichannel cross correlation (VanDecar and Crosson, 1990) in period bands using the finite-frequency kernels of Hung et al. (2000) to compute the sensitivities of band-limited delays. The process is similar to that of Schmandt and Lin (2014). For the purposes of this study, the S-wave velocity model, derived from inverting only body wave traveltimes via an LSQR inverse problem solver, is used as the jointly inverted model does not span the area of interest. The lack of local seismicity in the southern U.S. region suggests a heavy reliance on teleseisms, which provide poor depth resolution in the crust due to the nearly vertical, sub-parallel ray paths of teleseismic body waves.

PLH15

Porter et al. (2016) invert a combined Rayleigh wave dispersion dataset, derived from the USArray stations deployed between 2004 and April 2015, to produce a shear wave velocity model sensitive over a broad depth range. Rayleigh wave phase velocities are calculated using the ambient noise tomography method of Bensen et al. (2007) at short periods (8-40s) and the wave gradiometry technique of Liu and Holt (2015) at longer periods (20-150s). Dispersion curves for the combined phase velocity dataset are inverted using an iterative, linearized least squares inverse method (Herrmann and Ammon, 2002), with constant weights for each input phase velocity, a progressively decreasing damping factor, and a constant Vp/Vs ratio. The authors state that thick sediments along the Gulf coast increase uncertainties in the final S- wave velocity model.

PM15

The PM15 model of Pollitz and Mooney (2016) is a 3-D shear wave velocity model generated through the inversion of Rayleigh wave phase velocity maps, using broadband seismic data from USArray TA stations operating between April 2006 and December 2014. Rayleigh wave phase velocity maps are estimated from surface wave dispersion curves and 770,295 complex spectral amplitudes of fundamental mode surface wavetrains, obtained from 399 shallow-focus events, using the "nonplane wave" imaging methodology of Pollitz and Snoke (2010). Compared to higher modes, fundamental modes are primarily sensitive to near-surface structure.

SR16

SR16, by Shen and Ritzwoller (2016), derives from a set of vertical 1-D profiles beneath 1,816 USArray TA stations generated with a joint Bayesian Monte Carlo inversion of Rayleigh wave group and phase velocity from earthquakes and ambient noise, Rayleigh wave ellipticity (H/V) ratios from earthquakes, and receiver functions. The authors estimate uncertainties for each type of measurement used, with up to 0.04 km/s for phase velocities, 0.08 km/s for group velocities, and 3% for H/V measurements. The joint inversion technique of Shen et al. (2013) is used; it generates a posterior distribution of models that fit all measurements within tolerances that depend upon data uncertainties. The final shear velocity model is produced through a kriging interpolation of the mean of the posterior distribution of models. Uncertainties in crustal velocities are largest in the Mississippi Embayment, up to 0.20 km/s, with high values in the upper and lower crust.

SLK15

SLK15 (Schmandt et al., 2015) maps shear velocities of the crust and upper mantle, and Moho depths through multimode receiver function stacking, along with the inversion of Rayleigh wave phase velocity maps, created using Eikonal tomography (Lin et al., 2009) and Helmholtz tomography (Lin and Ritzwoller, 2011), and ellipticity, or H/V ratio, measurements. The multimode receiver function process creates a 3-D image by estimating P-S receiver functions, mapping receiver function time to depth using three forward-scattered modes (Ps, 2p1s, 2s1p) (Wilson and Aster, 2005), and CCP stacking (Dueker and Sheehan, 1997; Angus et al., 2009), using teleseismic P waveforms recorded at 2835 stations, including USArray stations up to June 2015 as well as temporary array and regional observatory stations. The inclusion of 2p1s and 2s1p seems to improve Moho depth estimates beneath sedimentary basins, where free surface multiples tend to interfere with Ps arrivals. To derive crustal thickness, the authors evaluate the Airy isostasy hypothesis using global reference values for density and topography and estimate crustal thickness values from the receiver function component of the study.

NA07

The NA07 model of Bedle and van der Lee (2009) is constructed with 5549 fundamental and higher-mode Rayleigh waveforms from 108 events, occurring from January 2000 through September 2006, using the Partitioned Waveform Inversion technique (van der Lee and Nolet, 1997). This is done through nonlinear fitting of observed seismograms, which are windowed and filtered to capture the direct, unscattered portion of the waveform, by synthetic waveforms constructed for each station-event path. A regularized linear inversion, using the LSQR algorithm of Paige and Saunders (1982), is performed to produce the 3-D S-wave velocity model relative to the 1-D reference model, MC35 (van der Lee and Nolet, 1997). Optimal regularization parameters are used, which neither decrease resolution nor introduce small-scale artifacts. The depth and lateral node spacing of the model is 20 km and 0.25°, respectively.

SL14

Using a 3D initial model based on surface waves, Schmandt and Lin (2014) invert 516,688 P and PKP traveltimes and 223,462 S and SKS traveltimes measured by multichannel cross-correlation (VanDecar and Crosson, 1990) in multiple frequency bands, using the frequency-dependent 3D sensitivity kernels method of Schmandt and Humphreys (2010). A linear inversion is performed using the LSQR algorithm of Paige and Saunders (1982). The authors use a variance reduction statistic to measure the quality of the model, for model parameters sampled by ray paths that span at least 120° of azimuth. The final model achieved a variance reduction of 75% for the S-wave residual times. The lateral and vertical grid spacing of the model, as used in this study, is 40-km and 30-50 km, respectively.

YFCR14

YFCR14 (Yuan et al., 2014) is an isotropic and radially anisotropic Vs model for the North American upper mantle using global and regional waveforms filtered at 60s and 40s, respectively. They derive 2D finite frequency waveform kernels (in the vertical plane) (Li and Romanowicz, 1996) by comparing Rayleigh and Love wave fundamental and overtone wave packets to synthetics via the non-linear asymptotic coupling theory of Li and Romanowicz (1995) for the 60s waveforms, and the spectral element method for the 40s waveforms. The model is parameterized by spherical splines, with depth and lateral node spacing of 10 km and 1-2°, respectively. Classical resolution analysis (e.g. Tarantola, 2005) is performed with synthetic models to illustrate the resolving power; expected lateral resolution is 200-400 km.

REFERENCES

Angus, D.A., Kendall, J.M., Wilson, D.C., White, D.J., Sol, S., and Thomson, C.J., 2009, Stratigraphy of the Archean western Superior Province from P- and S-wave receiver functions: Further evidence for tectonic accretion? Physics of the Earth and Planetary Interiors, v. 177, p. 206–216, doi:10.1016/j.pepi.2009.09.002.

Bedle, H., and van der Lee, S., 2009, S velocity variations beneath North America: Journal of Geophysical Research: Solid Earth, v. 114, p. B07308, doi:10.1029/2008JB005949.

Bensen, G.D., Ritzwoller, M.H., Barmin, M.P., Levshin, A.L., Lin, F., Moschetti, M.P., Shapiro, N.M., and Yang, Y., 2007, Processing seismic ambient noise data to obtain reliable broad-band surface wave dispersion measurements: Geophysical Journal International, v. 169, p. 1239–1260, doi:10.1111/j.1365-246X.2007.03374.x.

Dueker, K.G., and Sheehan, A.F., 1997, Mantle discontinuity structure from midpoint stacks of converted P to S waves across the Yellowstone hotspot track: Journal of Geophysical Research: Solid Earth, v. 102, p. 8313–8327, doi:10.1029/96JB03857.

Herrmann, R.B., and Ammon, C.J., 2002, Computer Programs in Seismology, Version 330. Saint Louis University, St Louis, Missouri:

Hung, S.-H., Dahlen, F.A., and Nolet, G., 2000, Fréchet kernels for finite-frequency traveltimeséII. Examples: Geophysical Journal International, v. 141, p. 175–203, doi:10.1046/j.1365-246X.2000.00072.x.

van der Lee, S., and Nolet, G., 1997, Upper mantle S velocity structure of North America: Journal of Geophysical Research: Solid Earth, v. 102, p. 22815–22838, doi:10.1029/97JB01168.

Li, X.-D., and Romanowicz, B., 1995, Comparison of global waveform inversions with and without considering cross-branch modal coupling: Geophysical Journal International, v. 121, p. 695–709, doi:10.1111/j.1365-246X.1995.tb06432.x.

Li, X.-D., and Romanowicz, B., 1996, Global mantle shear velocity model developed using nonlinear asymptotic coupling theory: Journal of Geophysical Research: Solid Earth, v. 101, p. 22245–22272, doi:10.1029/96JB01306.

Lin, F.-C., and Ritzwoller, M.H., 2011, Helmholtz surface wave tomography for isotropic and azimuthally anisotropic structure: Geophysical Journal International, v. 186, p. 1104–1120, doi:10.1111/j.1365-246X.2011.05070.x.

Lin, F.-C., Ritzwoller, M.H., and Snieder, R., 2009, Eikonal tomography: surface wave tomography by phase front tracking across a regional broad-band seismic array: Geophysical Journal International, v. 177, p. 1091–1110, doi:10.1111/j.1365-246X.2009.04105.x.

Liu, Y., and Holt, W.E., 2015, Wave gradiometry and its link with Helmholtz equation solutions applied to USArray in the eastern U.S.: Journal of Geophysical Research: Solid Earth, v. 120, p. 5717–5746, doi:10.1002/2015JB011982.

Obrebski, M., Allen, R.M., Pollitz, F., and Hung, S., 2011, Lithosphere–asthenosphere interaction beneath the western United States from the joint inversion of body-wave traveltimes and surface-wave phase velocities: Geophysical Journal International, v. 185, p. 1003–1021, doi:10.1111/j.1365-246X.2011.04990.x.

Paige, C.C., and Saunders, M.A., 1982, LSQR: An Algorithm for Sparse Linear Equations and Sparse Least Squares: ACM Transactions on Mathematical Software, v. 8, p. 43–71, doi:10.1145/355984.355989.

Pollitz, F.F., and Mooney, W.D., 2016, Seismic velocity structure of the crust and shallow mantle of the Central and Eastern United States by seismic surface wave imaging: Geophysical Research Letters, v. 43, p. 2015GL066637, doi:10.1002/2015GL066637.

Pollitz, F.F., and Snoke, A.J., 2010, Rayleigh-wave phase- velocity maps and three- dimensional shear velocity structure of the western US from local non-plane surface wave tomography: Geophysical Journal International, v. 180, p. 1153–1169, doi:10.1111/j.1365-246X.2009.04441.x.

Porritt, R.W., Allen, R.M., and Pollitz, F.F., 2014, Seismic imaging east of the Rocky Mountains with USArray: Earth and Planetary Science Letters, v. 402, p. 16–25, doi:10.1016/j.epsl.2013.10.034.

Porter, R., Liu, Y., and Holt, W.E., 2016, Lithospheric records of orogeny within the continental U.S.: Geophysical Research Letters, v. 43, p. 2015GL066950, doi:10.1002/2015GL066950.

Schmandt, B., and Humphreys, E., 2010, Complex subduction and small-scale convection revealed by body-wave tomography of the western United States upper mantle: Earth and Planetary Science Letters, v. 297, p. 435–445, doi:10.1016/j.epsl.2010.06.047.

Schmandt, B., and Lin, F.-C., 2014, P and S wave tomography of the mantle beneath the United States: Geophysical Research Letters, v. 41, p. 6342–6349, doi:10.1002/2014GL061231.

Schmandt, B., Lin, F.-C., and Karlstrom, K.E., 2015, Distinct crustal isostasy trends east and west of the Rocky Mountain Front: Geophysical Research Letters, v. 42, p. 2015GL066593, doi:10.1002/2015GL066593.

Shen, W., and Ritzwoller, M.H., 2016, Crustal and uppermost mantle structure beneath the United States: Journal of Geophysical Research: Solid Earth, v. 121, p. 2016JB012887, doi:10.1002/2016JB012887.

Shen, W., Ritzwoller, M.H., Schulte-Pelkum, V., and Lin, F.-C., 2013, Joint inversion of surface wave dispersion and receiver functions: a Bayesian Monte-Carlo approach: Geophysical Journal International, v. 192, p. 807–836, doi:10.1093/gji/ggs050.

Tarantola, A., 2005, Inverse Problem Theory and Methods for Model Parameter Estimation: SIAM, 349 p.

VanDecar, J.C., and Crosson, R.S., 1990, Determination of teleseismic relative phase arrival times using multi-channel cross-correlation and least squares: Bulletin of the Seismological Society of America, v. 80, p. 150–169.

Wilson, D., and Aster, R., 2005, Seismic imaging of the crust and upper mantle using regularized joint receiver functions, frequency–wave number filtering, and multimode Kirchhoff migration: Journal of Geophysical Research: Solid Earth, v. 110, doi:10.1029/2004JB003430.

Yuan, H., French, S., Cupillard, P., and Romanowicz, B., 2014, Lithospheric expression of geological units in central and eastern North America from full waveform tomography: Earth and Planetary Science Letters, v. 402, p. 176–186, doi:10.1016/j.epsl.2013.11.057.

FIGURES

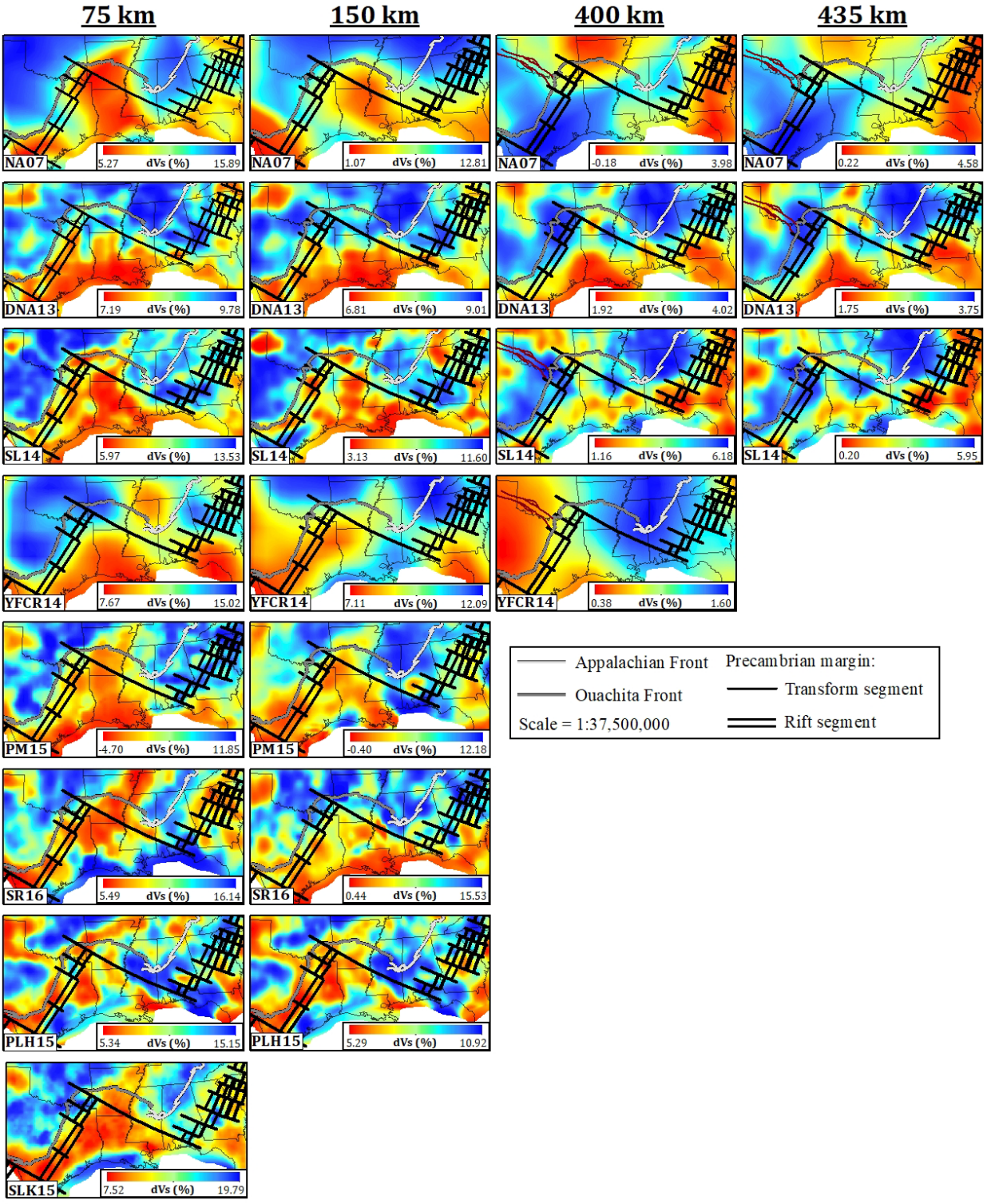

Figure DR1. Map view of shear velocity perturbations of models NA07, DNA13, SL14, YFCR14, PM15, SR16, PLH15, and SLK15 (rows; top to bottom) at 75-km, 150-km, 400-km, and 435-km depths (columns; left to right).

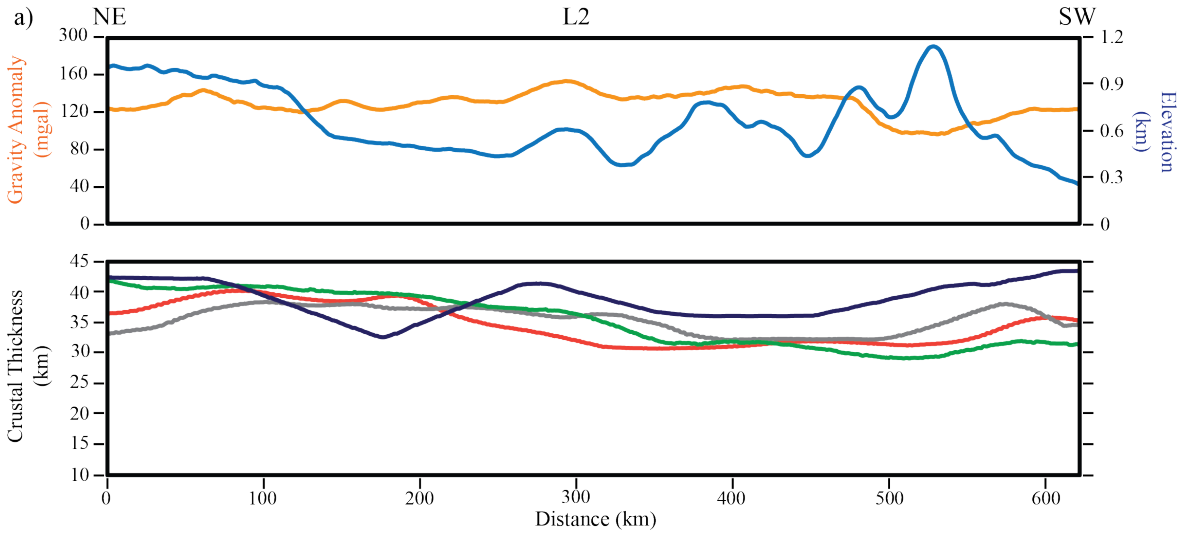
a)
NE
L2
SW
Gravity Anomaly (mgal)
Elevation (km)
Crustal Thickness (km)
Distance (km)

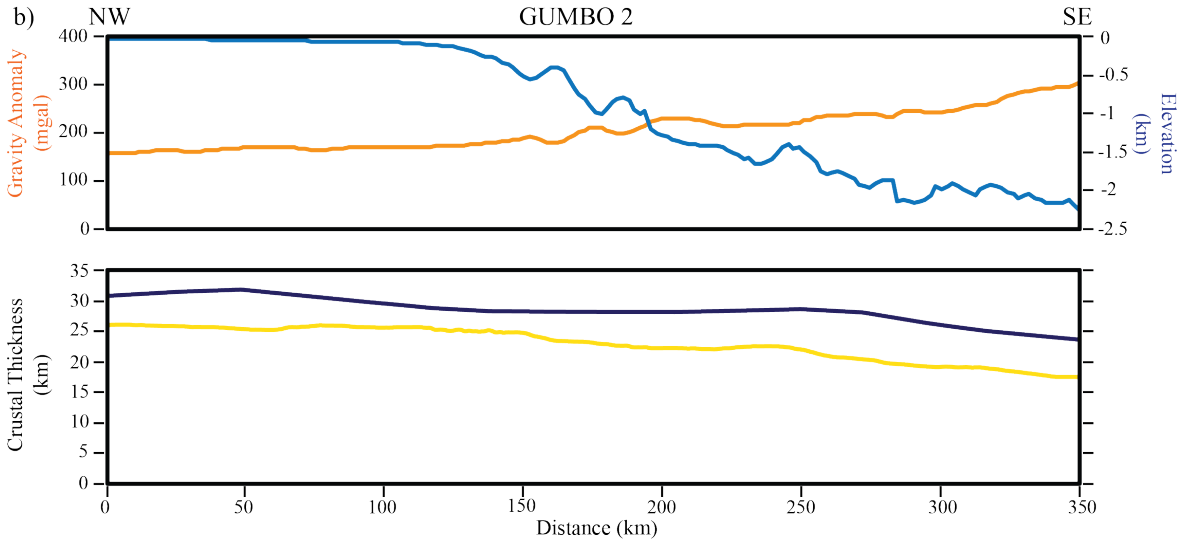
b)
NW
GUMBO 2
SE
Gravity Anomaly (mgal)
Elevation (km)
Crustal Thickness (km)
Distance (km)

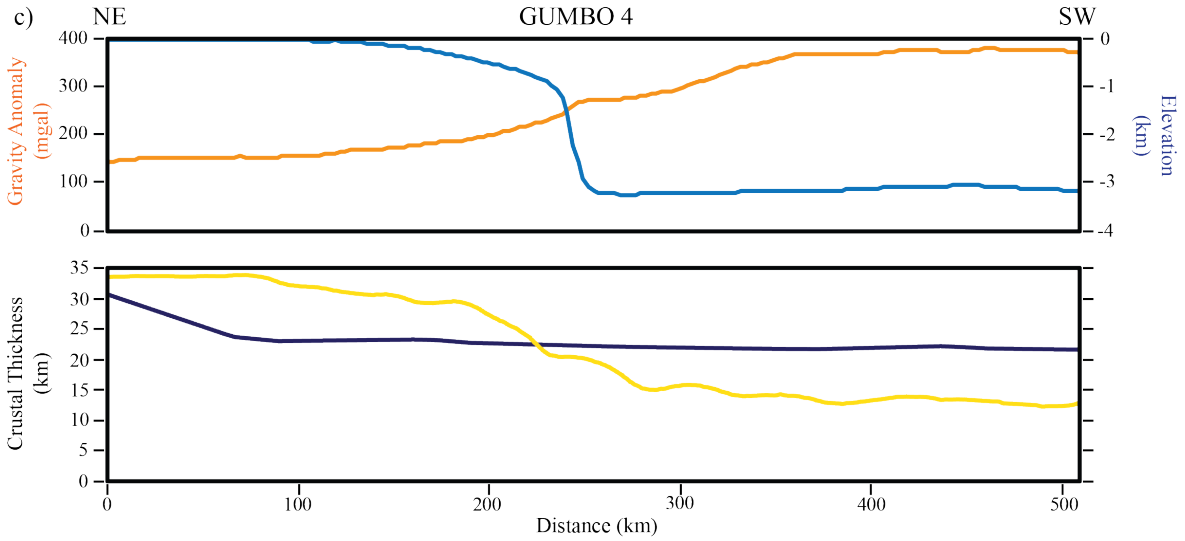
c)
NE
GUMBO 4
SW
Gravity Anomaly (mgal)
Elevation (km)
Crustal Thickness (km)
Distance (km)

Figure DR2. Cross-sectional profiles of a) L2, b) GUMBO2, and c) GUMBO4 lines (profile locations in Fig. 1), displaying lateral variation in Bouguer gravity anomaly (orange), topography (light blue), and crustal thickness based on models SR16 (green), SLK15 (grey), PnUS2016 (red), and LITHO1.0 (dark blue) along with results from the GUMBO studies (yellow).